Title: N-dihydrogalactochitosan reduces mortality in a lethal mouse model of SARS-CoV-2

Single Sentence Summary: The immunoadjuvant N-dihydrogalactochitosan diminishes SARS-CoV-2 disease in humanized ACE2 mice representing a new countermeasure against COVID-19.

Authors: Christopher M. Weiss[1,4], Hongwei Liu[1], Erin E. Ball[1], Samuel Lam[2], Tomas Hode[2], M. Kevin Keel[1], Richard M. Levenson[3], and Lark L. Coffey[1*]

[1] Department of Pathology, Microbiology & Immunology, University of California, Davis, CA

[2] Immunophotonics, Inc., Saint Louis, MO

[3] Department of Pathology and Laboratory Medicine, UC Davis Health, Sacramento, CA

[4] Current address: Meissa Vaccines, Inc., Redwood City, CA

*Corresponding Author

lcoffey@ucdavis.edu

ORCID iD:

Christopher Weiss 0000-0003-4704-9533

Hongwei Liu 0000-0002-8342-2545

Erin Ball 0000-0002-8464-6612

Richard Levenson 0000-0002-0112-6823

Lark Coffey 0000-0002-0718-5146

ABSTRACT

The rapid emergence and global dissemination of SARS-CoV-2 that causes COVID-19 continues to cause an unprecedented global health burden resulting in more than 4 million deaths in the 20 months since the virus was discovered. While multiple vaccine countermeasures have been approved for emergency use, additional treatments are still needed due to sluggish vaccine rollout and vaccine hesitancy. Immunoadjuvant compounds delivered intranasally can guide non-specific innate immune responses during the critical early stages of viral replication, reducing morbidity and mortality. N-dihydro**g**alacto**c**hitosan (GC) is a novel mucoadhesive immunostimulatory polymer of β-0-4-linked N-acetylglucosamine that is solubilized by the conjugation of galactose glycans. We tested GC as a potential countermeasure for COVID-19. GC administered intranasally before and after SARS-CoV-2 exposure diminished morbidity and mortality in humanized ACE2 receptor expressing mice by up to 75% and reduced infectious virus levels in the upper airway and lungs. Our findings demonstrate a new application for soluble immunoadjuvants like GC for preventing severe disease associated with SARS-CoV-2.

INTRODUCTION

Severe acute respiratory syndrome-like coronavirus 2 (SARS-CoV-2) that was first identified from a cluster of viral pneumonia cases in Wuhan, China in December 2019 *(1)* has caused more than 202 million cases and nearly 4.3 million deaths globally as of August 9, 2021. Clinical manifestations of 2019 novel coronavirus disease (COVID-19) caused by SARS-CoV-2 typically include fever, non-productive cough, and mild to moderate dyspnea, with severe cases developing pneumonia and acute respiratory distress syndrome *(1–3)*. SARS-CoV-2 morbidity and mortality increase with age and systemic proinflammatory and cardiovascular co-morbidities *(1, 2, 4)*. Recovered patients may also exhibit long-duration symptoms including disruption to sensations of taste and smell, and cognitive impairment (colloquially referred to as “brain fog”) resulting from neurological involvement *(5, 6)*.

Like SARS-CoV, SARS-CoV-2 uses the angiotensin converting enzyme 2 (ACE2) for cell entry *(7, 8)*. Small animals including mice, hamsters, and ferrets, have been fundamental in defining SARS-CoV-2 pathogenesis and developing medical countermeasures *(9, 10)*. Transgenic mice expressing the human ACE2 (hACE2) gene from the human cytokeratin 18 (K18) promoter have served as an especially useful model of severe disease due to well characterized genetics and ease of use *(11–13)*. Intranasal inoculation of K18-hACE2 mice (hereafter termed hACE2) with SARS-CoV-2 results in a high viral burden in the lungs, which diminishes past day 7, and elevated viral loads detectible in the brain at day 7 *(12)*.

SARS-CoV-2, which can be transmitted in small-droplet aerosols from person to person, can take up to 14 days to produce symptoms *(14)*. Public health countermeasures have evolved as additional treatments and information regarding transmission risks for COVID-19 have become available. In addition to face coverings and physical distancing, multiple vaccine candidates have now received emergency use authorization by the United States Food and Drug Administration (FDA) *(15)*. While ‘herd immunity’ through vaccination remains the target, it is estimated that 70-90% of the global population must be immune in order to interrupt

transmission *(16)*. This target becomes even more challenging with high levels of vaccine skepticism, slow production, inequitable distribution, and the rise of variants of concern capable of more efficient transmission or vaccine escape. Pre- and post-exposure countermeasures can help fill the vaccine gap by reducing COVID-19 morbidity and mortality in unprotected communities and thus reduce the global burden of the pandemic. The nucleoside analog remdesivir *(17)* is the only current FDA-approved therapeutic and was authorized based on its ability to shorten recovery time in COVID-19 patients *(18)*, but it is not ideal for clinical use due to its only moderate clinical efficacy *(19)*, as well as its requirement for intravenous administration. As of October 2020, there were nearly 400 active trials of therapeutic agents with more than 10 drugs or biological products holding emergency use authorization, mostly indicated for patients with severe COVID-19 *(20)*. Despite these advances, there are presently no drugs available for high-risk exposure use to protect against SARS-CoV-2. To circumvent this gap, we repurposed a therapy used for cancer and as a vaccine adjuvant with a goal of mitigating COVID-19 disease.

The parent compound of GC, chitosan, is a linear biological polysaccharide polymer of β-0-4-linked N-acetylglucosamine and is produced from alkaline treatment of the chitin exoskeleton of crustaceans. Chitosan is approved by the FDA for tissue engineering and drug delivery. Chitosan shows broad acting antiviral *(21)* and immunoadjuvant properties *(22, 23)* including interferon (IFN) induction *(24, 25)* that is critical for viral control *(26–28)*, and has been successfully tested as an antiviral therapy for respiratory viruses *(29–31)*. Modification of chitosan by attaching galactose molecules to the free amino acids on the polysaccharide backbone produces N-dihydro**g**alacto**c**hitosan (GC) *(32, 33)*. GC was initially designed to further improve immune stimulating function of the molecular backbone by adding glycan moieties, which can bind to C-type lectin receptors on antigen presenting cells *(34)* and lead to a downstream immune responses while retaining the mucoadhesive properties of the parent molecule *(35)*. Furthermore, GC has improved solubility at physiological pH ranges compared to

its parent molecule, and hence is more suitable as an injectable agent. With these modifications, GC has been developed for use in human interventional immuno-oncology to stimulate systemic anti-tumor immunity *(36)*. GC recruits granulocytes at the injection site *(37)* and stimulates activation of dendritic cells and macrophages through upregulation of co-stimulatory molecules CD40, CD86, and MHCII *in vitro* and *in vivo (38, 39)* . Macrophages also show increased nitric oxide production and phagocytic abilities *(38)*. Single-cell RNA sequencing indicates enrichment of type I IFN signaling in multiple innate immune cells, including monocytes, M1 macrophages, and neutrophils in tumors following GC administration *(40)*. Broad-acting non-toxic immunoadjuvants like GC that upregulate innate immune responses and recruit cellular responses to the exposure site represent a novel approach against SARS-CoV-2. Furthermore, non-specific immunoadjuvants such as GC could offer a benefit over more narrowly targeted antivirals by providing protection against a range of pathogens, potentially including future agents not yet affecting public health.

In the present study, we explored the use of GC for prophylaxis against SARS-CoV-2 infection applied pre- and post-exposure to lethal dosages of the virus in transgenic hACE2 mice. To simulate the use of solubilized GC as a nasal spray, we applied the compound intranasally twice before exposure and once following exposure of mice to a human isolate of SARS-CoV-2. Our data demonstrate a strong protective effect from GC in preventing mortality in this lethal model of disease. Pre- and post-exposure countermeasures can help fill the vaccine gap by reducing COVID-19 morbidity and mortality in unprotected communities and reduce the global burden of the pandemic.

RESULTS

N-dihydrogalactochitosan reduces SARS-CoV-2-associated mortality in hACE2 transgenic mice.

117 To determine the antiviral efficacy of N-dihydro**g**alacto**c**hitosan (GC) against SARS-
118 CoV-2, 6-week-old hACE2 [B6.Cg-Tg(K18-ACE2)2Prlmn/J] mice were treated intranasally (i.n.)
119 with 0.75% of GC in neutral buffered saline 3 and 1 days prior to virus exposure and 1 day post
120 exposure (**Fig. 1a**). Inhaled GC was well tolerated in mice, and no adverse events were noted
121 during or after treatment. Mice were challenged i.n. 1 day prior to the final GC treatment with 10^3
122 or 10^4 plaque forming units (PFU) of SARS-CoV-2, a route and dose intended to produce high
123 lethality in this model. Inocula were back-titrated to verify the administered dose. Tracheal
124 swabs were collected for the first 3 days post challenge and animals were monitored daily until
125 day 14 for weight loss and health status.

126 Weight remained stable for the first 3 days in all groups and infected controls rapidly
127 declined starting at day 4 in 10^4 PFU and day 5 in 10^3 PFU groups (**Fig. 1b**). Half of mice
128 experienced no weight loss throughout the duration of the study (**Supplementary Fig. 1**);
129 conversely, their growth outpaced mock-infected counterparts treated with saline alone
130 ($p<0.0001$). This effect was not limited to one biological sex and did not correlate with mouse
131 starting weight at the time of study initiation. Additional mice lost weight starting at day 4 but
132 failed to reach euthanasia criteria (loss of 20% of initial body weight) and recovered to starting
133 weight by day 14 post-challenge. Relative to the 10^4 group, mice challenged with 10^3 PFU
134 SARS-CoV-2 exhibited delayed or transient weight loss, with 1 mouse experiencing no weight
135 loss over the duration of the study. At the higher challenge dose of 10^4 PFU, GC significantly
136 reduced weight loss versus delivery vehicle treated controls ($p<0.0001$). At the lower 10^3 PFU
137 challenge dose, GC trended toward protection from weight loss, which was confounded by non-
138 uniform disease in delivery vehicle treated controls ($p=0.11$). Mice treated with delivery vehicle
139 and challenged with 10^3 or 10^4 PFU had a median survival time of 7±3.3 and 6.5±0.9 days,
140 respectively (**Fig. 1c**). At the lower challenge dose of 10^3 PFU, GC had an efficacy of 37.5%
141 protection from mortality ($p=0.05$) (**Fig. 1d**). At the higher challenge dose of 10^4 PFU, GC

142 reduced SARS-CoV-2 mortality by 75% (p<0.0001). Together, these results demonstrate the
143 potent efficacy of GC in preventing fatal SARS-CoV-2 disease in transgenic mice.
144

145 **N-dihydrogalactochitosan reduces SARS-CoV-2 viral levels in the upper respiratory tract.**
146 We next sought to determine whether GC reduced viral levels in addition to protecting mice from
147 mortality. Infectious SARS-CoV-2 levels were assessed longitudinally in mice by swabbing
148 throats from day 1 to 3 post-challenge (**Fig. 2a**). SARS-CoV-2 was detectible in the trachea of
149 infected animals at day 1 post challenge and most animals had no detectible virus by day 3.
150 Virus levels were elevated in mice inoculated with 10^4 PFU versus 10^3 PFU at 1 day post
151 challenge (p=0.05), but differences between challenge doses were not detected after day 2
152 (p>0.99). GC significantly reduced virus levels in the trachea at day 1 and day 2 post challenge
153 with 10^4 PFU (p=0.0005 and p=0.02, respectively). A similar effect was not observed in mice
154 receiving the lower inoculum of 10^3 PFU. All delivery vehicle-treated mice had detectible virus in
155 swabs following infection, while 29.2% (7/24) of mice had no infectious virus isolated between
156 days 1 and 3. Positive virus detection in tracheal swabs was not correlated with lethal disease in
157 mice (p=0.62, Fisher's exact test). Cumulative virus levels in tracheal swabs were calculated as
158 area under the curve for individual animals (**Fig. 2b**). GC significantly reduced the total virus
159 levels in mice challenged with 10^4 PFU from a geometric mean of 225 to 5.6 PFU collected in
160 swabs (p<0.0001) and trended toward a reduction in animals challenged with 10^3 PFU from 138
161 to 15 PFU collected in swabs (p=0.08).
162 As individual animals met humane experimental endpoints, mice were euthanized
163 between days 5 and 7. Infectious virus levels were measured in the lungs (**Fig. 2c**) and brain
164 (**Fig. 2d**) at the time of death. The geometric mean lung viral titers ranged from 89 to 1209
165 PFU/mg in delivery vehicle-treated control animals. Similarly, GC-treated mice had geometric
166 mean lung titers ranging from 6 to 1004 PFU/mg. GC treatment trended toward a reduction in

167 lung virus levels (F=2.431, p=0.06, two-way ANOVA) with cumulative effects in animals
168 challenged with 10^3 PFU driving the main treatment effect (p=0.06).
169 Comparatively high viral titers were observed in the brain at the time of death, consistent
170 with previous descriptions in this model *(12)*. Virus was detectible in the brain in all but 2
171 infected animals at the time of death, indicating neuroinvasion as a likely cause of morbidity.
172 Delivery vehicle-treated control animals had geometric mean brain titers ranging from 13,695 to
173 21,4045 PFU/mg. Geometric mean brain titers in GC-treated animals ranged from 1,351 to
174 24,299 PFU/mg. No significant trends in brain virus levels were observed between treatments
175 (F=0.8134, p=0.52, two-way ANOVA). No infectious virus was detectible in the lungs or brains
176 of animals euthanized at day 14 post challenge.
177 **N-dihydrogalactochitosan reduces the severity of histopathologic lesions associated**
178 **with SARS-CoV-2 infection in lungs.**
179 Intranasal inoculation of hACE2 transgenic mice with PBS followed by mock inoculation
180 resulted in normal lung architecture in most mice, although several animals exhibited mild
181 alveolar septal inflammation, likely associated with i.n. administration **(Fig. 3a)**. By contrast,
182 mice inoculated with 10^3 or 10^4 PFU SARS-CoV-2 (**Fig. 3c**, representative 10^3 image shown)
183 exhibited extensive lymphohistiocytic interstitial pneumonia with a peribronchiolar and
184 perivascular distribution and scattered multinucleated syncytial cells. Bronchiolitis, bronchiolar
185 epithelial and alveolar septal necrosis, hemorrhage, fibrin, edema, and vascular endothelial
186 inflammation were also occasionally noted. SARS-CoV-2-infected mice treated with GC showed
187 lesser histopathologic lesions in the lung (**Fig. 3b**) compared to animals that did not receive GC,
188 and inflammation was focally distributed instead of widespread. To quantify histopathologic
189 changes, lung lesion severity (**Fig. 3d**) was scored using specific criteria (**Supplementary**
190 **Table 1**) and the total area of the lung that was affected was estimated using image analysis
191 software (**Fig. 3e**). GC treatment significantly reduced the mean severity score for animals
192 dosed with 10^4 PFU SARS-CoV-2 from 4.6 to 2.5 (ANOVA, $p < 0.0001$). Mean scores for mice

193 treated with GC and 10^3 PFU of SARS-CoV-2 trended towards being lower than for mice who
194 did not receive GC but were not significantly different ($p > 0.05$). The percent of lung affected in
195 mice that received the 10^4 SARS-CoV-2 dose was also significantly reduced from a mean of
196 33% to 13% ($p < 0.0001$); differences at the 10^3 dose were not significant.

197 A subset of GC-treated and untreated mice exhibited mild rhinitis, characterized by
198 mucus, sloughed cells, necrotic debris, and scattered neutrophils in the nasal cavity. One GC-
199 treated mouse (**Supplementary Fig. 2a**) and 3 mock-inoculated mice exhibited pulmonary
200 foreign-material reactions, with necrosuppurative bronchiolitis and multiple foci of neutrophils,
201 macrophages, and multinucleated giant cells surrounding intracellular and extracellular brightly
202 eosinophilic foreign material. Consistent with high viral titers in the brain, some GC-treated and
203 untreated mice exhibited mild to moderate lymphocytic meningitis with perivascular cuffing and
204 occasional extension of lymphocytes into the adjacent neuropil (**Supplementary Fig. 2b,c**).
205 Together, these data show that GC reduces SARS-CoV-2-induced disease in the lung of
206 hACE2 mice, although only significantly in mice administered the higher 10^4 PFU dose of
207 SARS-CoV-2. The pulmonary foreign material reactions and alveolar inflammation in both GC-
208 and mock-treated mice may stem from the volume or frequency of i.n. treatment; future studies
209 using GC could modify both parameters as a means to reduce these lesions.

210 **Mice treated with N-dihydrogalactochitosan produce neutralizing antibodies after SARS-**
211 **CoV-2 exposure.**

212 Finally, we sought to determine whether mice surviving SARS-CoV-2 challenge
213 produced a humoral immune response that might protect them from future challenge. Serum
214 from blood collected at day 14 post inoculation was assessed for neutralizing antibody against
215 the challenge strain of SARS-CoV-2 by plaque reduction neutralization test (PRNT) at the 80%
216 neutralization threshold (**Fig. 4**). All infected mice surviving viral challenge generated
217 neutralizing antibodies. Mice in the GC group challenged with 10^3 or 10^4 PFU generated
218 geometric mean neutralizing titers of 1:676 and 1:861, respectively. In comparison, PBS-

219 administered mice that received a challenge dose of 10^3 PFU had a mean neutralizing titer of
220 1:1448. Neutralizing antibody titers were not different across treatments ($p>0.9999$) or virus
221 dose, although PBS-administered mice challenged with 10^4 PFU SARS-CoV-2 were unavailable
222 for comparison due to uniform lethality. These data confirm that surviving mice were
223 productively infected and indicate that animals were able to develop adaptive immune
224 responses that could potentially protect against reinfection.
225

226 **DISCUSSION**

227 Intranasal administration of GC to prevent or treat SARS-CoV-2 represents a novel
228 application of this potent immunostimulatory compound. In the present study, GC was well-
229 tolerated and prevented lethal disease in up to 75% of treated humanized mice, while all mice
230 not receiving GC but challenged with the 10^4 PFU SARS-CoV-2 had to be euthanized. All
231 surviving animals had neutralizing antibodies detectable at 14 days post inoculation. Similar
232 SARS-CoV-2 antibody titers were detected in GC-treated and untreated animals. Mice that
233 received GC treatment also displayed lower levels of infectious SARS-CoV-2 in tracheal swabs
234 collected 1 to 2 days post inoculation and had less severe lesions in lungs. Reducing virus
235 levels in the upper airway has gained particular significance as recent vaccine breakthrough
236 cases with variants of concern demonstrate SARS-CoV-2 shedding at similar levels to
237 unvaccinated individuals, which is a key determinant of transmission potential *(41)*. Our findings
238 demonstrate a reduction in viral burden and virus-induced disease along with a resultant
239 increase in survival due to GC treatment.

240 GC is a polymeric mixture containing strands of varying lengths of selectively galactose-
241 conjugated and partially deacetylated β-0-4-linked N-acetylglucosamine molecules with a
242 specific range of molecular weights *(32, 33, 36, 37)*. Synthesized and purified under Good
243 Manufacturing Practice (GMP) conditions, N-dihydrogalactochitosan is a well-characterized
244 variant of GC. Characterization and quality control testing ruled out contamination from

245 endotoxins, heavy metals, and other impurities, which eliminates a major confounding factor in
246 the research of these naturally derived molecules, and chitosan in particular *(42)*. Water
247 solubility, immunological properties, biocompatibility, and a favorable toxicity profile are key
248 features of GC. The unconjugated base polymer, chitin, is a primary structural component of cell
249 walls for organisms ranging from fungi to arthropods *(21)*. Chitosan, a derivative of chitin, is
250 deacetylated through alkaline treatment and is marketed as a nutritional supplement *(43)* and
251 used as a biopolymer *(44)*. Unmodified chitosan has been used successfully to treat influenza A
252 virus infection in mice *(29)*, demonstrating a potential application as a non-specific antiviral
253 compound for respiratory virus infection. However, unmodified chitosan has low solubility in
254 neutral buffered aqueous solution and requires acidic formulation; poor characterization,
255 purification and lack of controlled synthetic process leads to poor reproducibility and
256 unpredictable outcomes *(42)*. GC circumvents these limitations through a controlled and
257 reproducible process of synthetically attaching galactose to the free-amino groups of the
258 chitosan base, improving solubility (and thus bioavailability) while maintaining a physiological
259 pH. GC has been previously used as a combination anti-tumor therapy due to its
260 immunoadjuvant properties *(38, 40)*, but its utility as a broad-acting antiviral compound has not
261 previously been investigated.

262 Immunoadjuvants stimulate non-specific innate immune responses through various
263 mechanisms. Some use pattern-recognition receptors, including the Toll-like receptor (TLR)
264 family of antigen detection complexes. While the mechanism of SARS-CoV-2 protection has not
265 been determined for GC, chitosan, and similar polymers of N-acetylglucosamine, interact with
266 TLR2, which serves as a rationale for inclusion of chitosan as a vaccine adjuvant. TLR2 signals
267 through myeloid differentiation factor 88 (MyD88) to stimulate the nuclear factor kappa B (NF-
268 κB) pathway and downstream inflammatory and anti-microbial cytokine responses *(45, 46)*. TLR
269 engagement of the canonical NF-κB pathway up-regulates both tumor necrosis factor alpha
270 (TNF-α) and interleukin-6 (IL-6), two potent pro-inflammatory effectors. IL-6, which is necessary

271 for antiviral immunity against other virus families, has been identified as a target of
272 dysregulation associated with hyperinflammatory responses in the lungs during SARS-family
273 coronavirus infections. SARS-CoV-1 nucleocapsid protein can stimulate NF-κB activation and
274 IL-6 production independent of infection *(47)*. Prolonged high levels of IL-6 are correlated with
275 severe COVID-19 outcomes in humans, and a similar association has been found in ferrets
276 infected with SARS-CoV-2 *(48)*. The timing of IL-6 production may play a critical role in
277 determining whether viral clearance is achieved or alternatively, hyperinflammatory responses
278 result. Early, but not late, induction of IL-6 during respiratory syncytial virus (RSV), influenza A,
279 and rhinovirus infection promote viral clearance and limit prolonged inflammation by establishing
280 regulatory T cell populations that limit virus spread *(49)*. Similarly, timed induction of pro-
281 inflammatory responses by GC treatment pre- and post-infection may promote viral clearance
282 before virus-mediated dysregulation of this pathway can occur. As such, future studies should
283 explore the timing of GC treatment and regulation of IL-6 and associated pro-inflammatory
284 pathways.

285 The data in this study demonstrate that treatment with GC induces robust neutralizing
286 antibody responses by day 14, after a reduction in infectious SARS-CoV-2 in tracheal swabs by
287 day 3. These data suggest GC functions as an immunoadjuvant that can modulate innate
288 immune responses after SARS-CoV-2 infection, leading to stimulation of robust antiviral
289 adaptive immunity. Experimental evidence from cell culture and animal models support at least
290 three mechanisms by which complex carbohydrates such as GC could stimulate the innate and
291 adaptive immune systems *(50–53)*. First, GC recognition by sensors on macrophages and
292 dendritic cells (DC) can stimulate innate immune defenses *(54–56)*. While immune receptors for
293 GC have not been identified, chitosan binding to C-type lectin receptors such as dectin-1 can
294 initiate innate immune signaling *(57, 58)*. Second, GC-mediated antigen uptake *(59)* and antigen
295 presentation by DCs could lead to CD4 and CD8 T cell responses *(37, 38)*. Studies in mice
296 show GC induces type 1 IFN *(40)*, leading to enhanced DC activation and robust CD4 T helper

297 cells *(51)*. Notably, DNA sensor activation is mediated via cellular DNA release by chitosan.
298 Third, physical antigen sequestration and slow antigen release within draining lymph nodes
299 facilitated by GC could potentially prolong germinal center reactions, thereby enhancing
300 humoral immunity by fostering affinity maturation of B cells *(60, 61)*. Thus, GC may have
301 potential as a dual-purpose preventative and therapeutic with immunostimulatory properties.
302 Future studies are needed to investigate the impact of GC on SARS-CoV-2-specific immune
303 responses.

304 In addition to the immunoadjuvant properties of GC, direct interactions between GC and
305 SARS-CoV-2 in the nasal cavity may contribute to the protection we observed in mice. As the
306 nasopharyngeal and oral cavity are often the primary entry sites of SARS-CoV-2 and other
307 respiratory viruses, interventions or medications at these locations could provide an important
308 boost in the first line of defense. The reduction in SARS-CoV-2 levels in GC treated mice in the
309 first 2 days post-challenge suggests that GC has early effects that hamper the initial phase of
310 viral infection, especially given that serum neutralizing antibodies are not detectable before
311 about 7 days. In addition to possible innate immune stimulation, aqueous GC is viscous and
312 may remain in the airway after intranasal administration. GC present at the time of infection may
313 act as a physical barrier or directly inactivate SARS-CoV-2 before it can initiate infection.
314 Additional studies of GC bioavailability and detailed studies of GC-virus interactions including to
315 establish whether GC blocks virus entry and/or replication are needed to establish mechanisms
316 of protection; these experiments could also clarify why greater protection from lethal disease
317 was observed after challenge with the higher SARS-CoV-2 dose in these studies.

318 In summary, we show here that GC treatment of humanized mice pre- and post-infection
319 with SARS-CoV-2 reduces lethal disease, virus levels in the upper respiratory tract, and
320 significant lesions in the lungs. These data suggest a possible role of GC as a SARS-CoV-2
321 countermeasure. Additional pre-clinical studies could focus on the mechanism of protection,
322 including further assessment of the antiviral and immunomodulatory effects of GC. Future

323 studies should also identify the GC dose and schedule that confer the greatest benefit in
324 reducing disease while minimizing foreign-material reactions as detected in the lungs of several
325 of the mice in this study, as well as to determine whether GC shows both prophylactic and
326 therapeutic benefits.
327

328 **METHODS**

329 ***Ethics Statement:*** All mouse work was conducted on protocol #21868 approved by the
330 institutional animal care and use committee (IACUC) at the University of California, Davis.
331 Infectious virus was handled in certified animal biosafety level 3 laboratory (ABSL-3) spaces in
332 compliance with approved institutional biological use authorization #R2813. The University of
333 California, Davis, is accredited by the Association for Assessment and Accreditation of
334 Laboratory Animal Care (AAALAC). All mouse work adhered to the NIH Guide for the Care and
335 Use of laboratory Animals.

336 ***Mice:*** Equal numbers of male and female transgenic mice expressing the human ACE2
337 receptor on a K18 transgene in a C57Bl/6J background (B6.Cg-Tg(K18-ACE2)2Prlmn/J,
338 referenced as 'hACE2') were purchased at 5 weeks of age from Jackson Laboratories
339 (Sacramento, CA). Mice were co-housed by sex in ABSL-3 conditions with 4 animals per cage
340 and acclimated for up to 6 days at 22-25°C and a 12:12 hour light: dark cycle. Rodent chow with
341 18% protein content and sterile bottled water was provided *ad libitum* for the duration of the
342 experiment.

343 ***Virus:*** SARS-CoV-2/human/USA/CA-CZB-59X002/2020 (GenBank #MT394528), which was
344 isolated from a patient in 2020 in Northern California and passaged once in Vero-E6 cells, was
345 generously provided by Dr. Christopher Miller (University of California, Davis). To generate
346 stocks for these studies, SARS-CoV-2 was passaged one additional time in Vero-E6 cells to
347 achieve a titer of 2.2 x 10^7 plaque forming units (PFU)/mL. Single-use virus aliquots were stored
348 at -80°C.

349 ***N-dihydrogalactochitosan Treatment and SARS-CoV-2 Challenge*:** Sterile 1%
350 weight/volume N-dihydrogalactochitosan (GC) was provided by Immunophotonics. GC was
351 generated using Good Manufacturing Practices (GMP). Testing of GC included appearance,
352 identity (1H NMR and UV/Vis), assay (HPLC), degree of galactation (1H NMR), viscosity,
353 specific gravity, pH, microbiological (endotoxins and sterility), subvisible particulate matter,
354 impurities (boron, galactose, galactitol, transition metals), molecular weight, and polydispersity
355 indices. GC was presented as a 1.0% sterile solution (10 mg/ml) in 5 ml sealed vials and was
356 diluted with sterile deionized water and sterile filtered 20X phosphate buffered saline (PBS) to a
357 final concentration of 0.75% GC and 1X PBS. Mice were anesthetized with isoflurane and 40 µL
358 of either diluted GC or PBS delivery vehicle was administered intranasally (i.n.) by a hanging
359 drop over both nares. Mice were treated identically at 3 days and 1 day prior to challenge and 1
360 day post challenge. At challenge, mice were anesthetized and administered 30 µL of PBS or
361 SARS-CoV-2 diluted in PBS at a dose of 10^3 or 10^4 PFU i.n. via hanging drop. Inocula were
362 back-titrated to confirm the target dose. Mice were monitored twice daily for changes in weight,
363 ruffled fur, ataxia, and labored breathing for up to 14 days. On days 1, 2 and 3, mice were
364 anesthetized with isoflurane and throats were swabbed with rayon-tipped swabs (Puritan, Fisher
365 Scientific, Fisher Scientific, Waltham, MA). Swabs were vortexed briefly in 400 µL of Dulbecco's
366 Modified Eagles Medium (DMEM, Fisher Scientific, Waltham, MA) and frozen at -80°C. Mice
367 were euthanized prior to experimental endpoint if weight loss exceeded 20% of the starting
368 weight or if animals were deemed moribund as evidenced by limb weakness, ataxia or dragging
369 of limbs, loss of limb function or rapid or depressed respiration rate. An adverse event was
370 defined as any moribund disease signs at any time over the duration of the experiment. Prior to
371 euthanasia, whole blood was collected by submandibular vein puncture under isoflurane
372 anesthesia. Whole blood was clotted for >10 min at room temperature then centrifuged for 5
373 minutes at 8,000 x g and cleared serum was stored at -80°C. Mice were euthanized by
374 isoflurane overdose and cervical dislocation then perfused with cold sterile PBS. Lung (right

375 inferior lobe) and brain (left hemisphere) were weighed and homogenized in 1-10 µL/mg DMEM
376 with a sterile glass bead at 30 Hz for 4 minutes using a TissueLyser (Qiagen, Germantown, MD)
377 automated homogenizer. Homogenates were cleared by centrifugation at 10,000 x g for 4
378 minutes and the cleared fraction was stored at -80°C.

379 ***Histopathology*:** At necropsy, lungs were inflated with 10% buffered formalin (Fisher Scientific,
380 Waltham, MA) and mice were fixed for 48 hours at room temperature in a 10-fold volume of
381 10% buffered formalin. Skulls were demineralized in a 10-fold volume of 0.5 M ethylenediamine
382 tetraacetic acid (EDTA) (pH=7) at 4°C for 14 days, with EDTA solution exchanges every 3 days.
383 Tissues were embedded in paraffin, thin-sectioned, and stained with hematoxylin and eosin
384 (H&E). H&E-stained slides were scanned by a whole-slide image technique using an Aperio
385 slide scanner (Leica, Buffalo Grove, IL) with a resolution of 0.24 µm/pixel. Image files were
386 uploaded on a Leica hosted web-based site and a board certified veterinary anatomic
387 pathologist without knowledge of treatment conditions evaluated sections for SARS-CoV-2
388 induced histologic lesions. For quantitative assessment of lung inflammation, digital images
389 were captured and analyzed using ImageJ software (Fiji, NIH) to estimate the area of inflamed
390 tissue that was visible to the naked eye at subgross magnification as a percentage of the total
391 surface area of the lung section. Each lung section was scored as described (**Supplementary**
392 **Table 1**).

393 ***Plaque Assay*:** Washes from tracheal swabs, serum, residual inocula, and lung and brain
394 homogenates were thawed and assayed. Samples were serially diluted 10-fold in DMEM with
395 1% bovine serum albumen (BSA) starting at an initial dilution of 1:8. 125 µL of each dilution was
396 added to confluent Vero CCL-81 cells (ATCC, Manassas, VA) in 12-well plates with cell culture
397 media decanted. Virus was incubated on cells for 1 hour at 5% CO2 in a humidified 37°C
398 incubator. Cell monolayers were overlaid with 0.5% agarose dissolved in DMEM with 5% fetal
399 bovine serum (FBS) and 1x antibiotic-antimycotic (Fisher Scientific, Waltham, MA) and
400 incubated for 3 days at 5% CO2 and 37°C in a humidified incubator. Cells were fixed for >30

401 minutes with 4% formaldehyde then agarose plugs were removed. Cells were stained with
402 0.05% crystal violet in 20% ethanol for 10 minutes then rinsed three times with water. Plates
403 were inverted to dry completely and the number of plaques in each well was counted. Viral titers
404 were recorded as the reciprocal of the highest dilution where plaques were noted and are
405 represented as PFU per swab or PFU per mg of solid tissue.

406 ***Plaque Reduction Neutralization Test*:** Serum collected from mice at day 14 post inoculation
407 was thawed at 37°C and 30 µL was heated in a water bath for 30 minutes at 56°C to inactivate
408 complement proteins. Serum was diluted 4-fold with virus diluent consisting of PBS and 1%
409 FBS, then samples were serially 2-fold diluted 11 times for a dynamic range of 1:4 to 1:4096. An
410 equal volume of virus diluent containing 80 PFU of SARS-CoV-2 was added to each antibody
411 dilution and a no-antibody control consisting of virus diluent only, resulting in a final dynamic
412 range of 1:4 to 1:8192 with one no-antibody control. Antibody-virus dilution series were
413 incubated for 1 hour at 37°C after which they were applied to confluent Vero CCL-81 cells in
414 single-replicate and incubated for 1 hour at 5% CO2 and 37°C in a humidified incubator. Cells
415 were overlaid, incubated, fixed, and stained as described above for plaque assays. Neutralizing
416 titer is defined as the reciprocal of the dilution for which fewer than 20% of plaques were
417 detected versus the no-antibody control (>80% neutralization).

418 ***Statistics*:** All statistical tests were performed with GraphPad PRISM 9.0.2 (GraphPad
419 Software). Logrank (Mantel-Cox) test for survival proportions were performed pairwise and *p*-
420 values were adjusted with Bonferroni correction using R version 4.0.0 (R Project) p.adjust
421 function. The correlation between mortality and positive virus detection was calculated by
422 Fisher's exact test. Repeated measures two-way ANOVA tests were performed on log10-
423 transformed viral titers and multiple comparisons were computed according to Tukey method.
424 Main effect two-way ANOVA tests were performed on mouse weights normalized to starting
425 values at the time of virus challenge or log10-transformed viral titers and multiple comparisons
426 were computed with Tukey's method. Area under the curve (AUC) was calculated for

427 longitudinally collected tracheal swabs from days 1,2 and 3 and log10-transformed. ANOVA of
428 grouped log10-AUC was performed with multiple comparisons computed with Tukey's method.
429 ANOVA was performed on untransformed histologic scores or percentage of lung affected by
430 inflammation and multiple comparisons were computed with Bonferroni's method. A Kruskal-
431 Wallis H test was performed on untransformed PRNT80 neutralization values and multiple
432 comparisons were computed according to Dunn's method.
433

434 **DATA AVAILABILITY**

435 All data contributing to the generation of figures and analyses described herein are available
436 upon request from the corresponding author.
437

438 **COMPETING INTERESTS**

439 TH and SSKL declare a conflict of interest as employees with minority ownership stakes of
440 Immunophotonics, Inc., the manufacturer of the proprietary immune stimulant GC. RML
441 declares a conflict of interest as an advisor with minority ownership stake in Immunophotonics.
442

443 **AUTHOR CONTRIBUTIONS**

444 Conceptualization: RML, LLC, TH, SSKL, CMW, HL, and EEB. Investigation: CMW, HL, and
445 EEB. Writing draft: CMW. Review and editing: CMW, HL, EEB, LLC, TH, SSKL,MKK, and RML.
446 Visualization: CMW, EEB, MKK, LLC. Supervision and project administration: LLC. Funding
447 acquisition: RML and LLC.
448

449 **ACKNOWLEDGEMENTS**

450 Funding support was provided by the UC Berkeley Henry Wheeler Center for Emerging and
451 Neglected Diseases (CEND) COVID Catalyst Fund, and internal funding from the UC Davis

Office of the Vice Chancellor of Research. Funding sources did not influence experimental design and analysis/interpretation of results or impact the decision to publish.

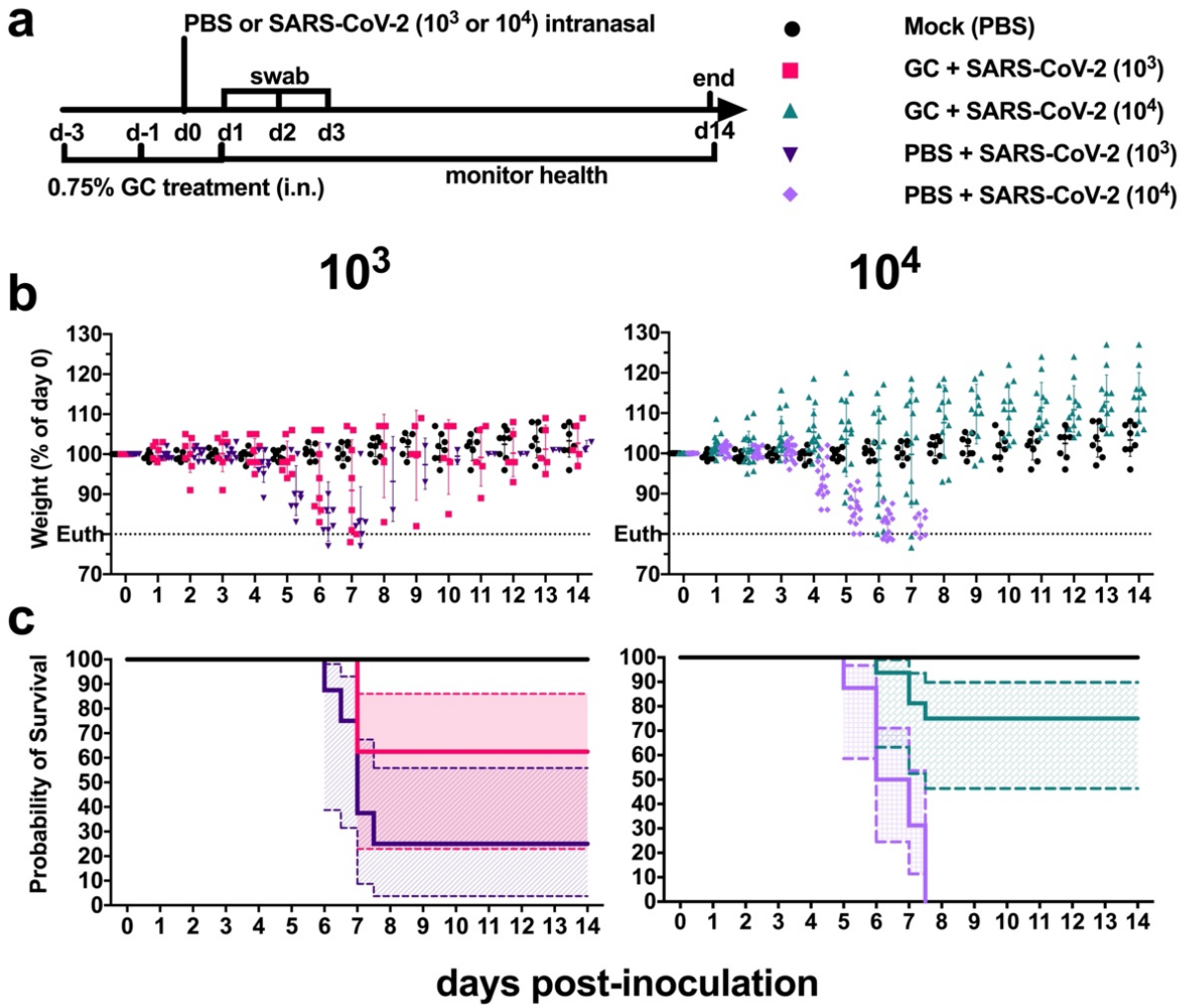

d **Survival comparisons**

GROUP 1	GROUP 2	P VALUE	SIGNIFICANCE
mock	GC + SARS-CoV-2 (10^3)	0.5024	ns
mock	GC + SARS-CoV-2 (10^4)	1.0000	ns
mock	SARS-CoV2 (10^3)	0.0200	*
mock	SARS-CoV-2 (10^4)	0.0001	****
GC + SARS-CoV-2 (10^3)	GC + SARS-CoV-2 (10^4)	1.0000	ns
GC + SARS-CoV-2 (10^3)	SARS-CoV2 (10^3)	0.0504	ns
GC + SARS-CoV-2 (10^4)	SARS-CoV-2 (10^4)	0.0001	****
SARS-CoV2 (10^3)	SARS-CoV-2 (10^4)	1.0000	ns

Fig. 1: N-dihydrogalactochitosan protects mice from SARS-CoV-2 mortality. (a) Experimental design where 6-week-old male and female hACE2 transgenic mice were treated with 0.75% GC or PBS delivery vehicle at days -3, -1 and +1 post-inoculation. Mice were challenged at day 0 with 10^3 or 10^4 PFU of SARS-CoV-2 or PBS (mock). Animals were weighed

459 daily, and throats were swabbed on days 1 through 3. (**b**) **Weight** represented as a percentage
460 of individual mouse weight at the time of challenge. Euth = euthanasia cutoff. A main effect only
461 model two-way ANOVA with Tukey corrected multiple comparisons yielded an F=52.80,
462 p<0.0001, 4 degrees of freedom. Each symbol represents an individual mouse, and the
463 horizontal lines show geometric mean and error bars are geometric standard deviation. **(c)**
464 **Survival proportions.** The solid lines are survival proportions, and the shaded boxes show
465 95% confidence intervals. **(d) Logrank Mantel-Cox comparisons of survival proportions**
466 with Bonferroni corrected p-values, multiple pairwise tests, 1 degree of freedom. n=8-16 per
467 group, 2 combined experiments.

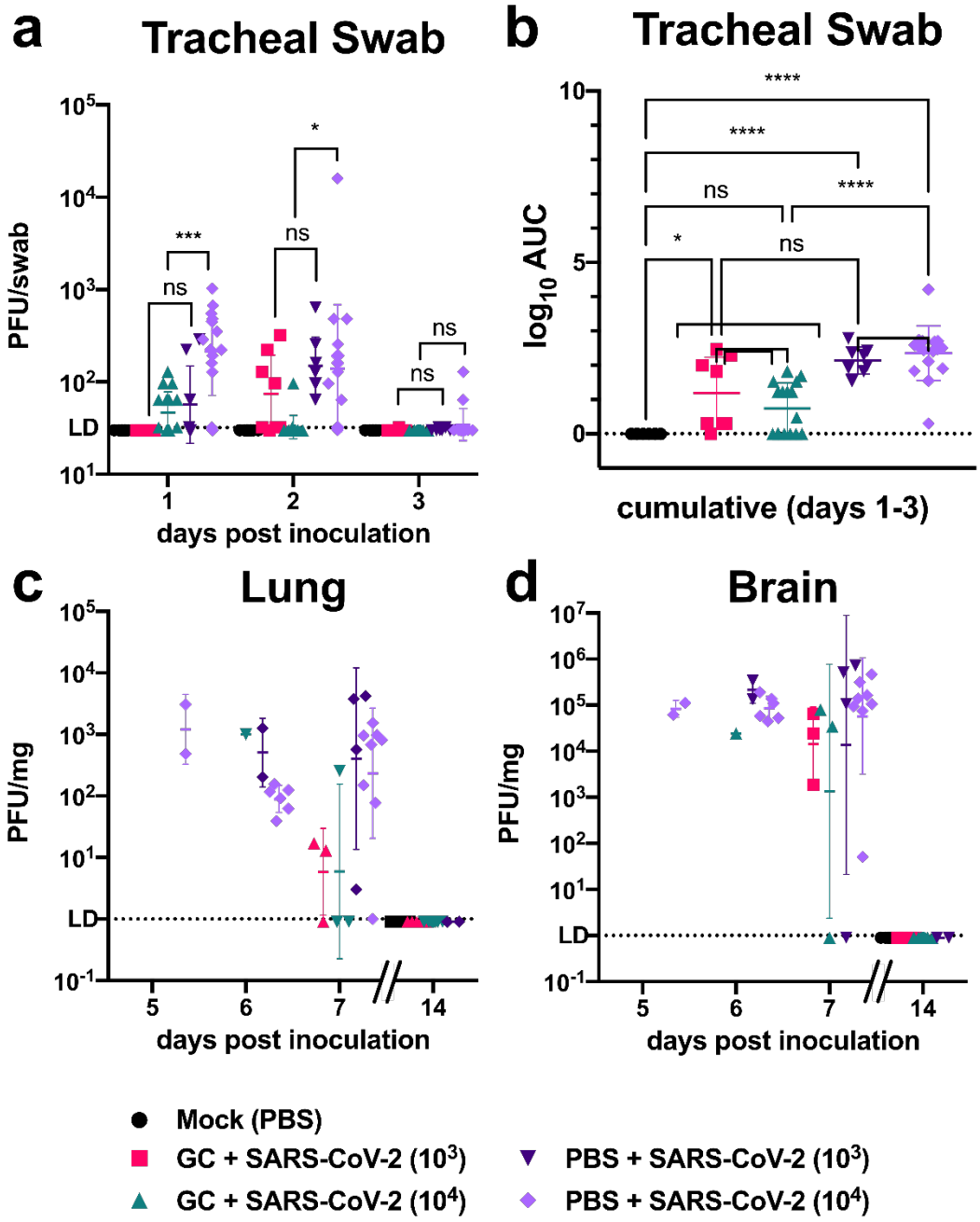

Fig. 2: N-dihydrogalactochitosan reduces SARS-CoV-2 detection in the upper respiratory tract. Infectious SARS-CoV-2 was measured in (**a**) **tracheal swabs** collected from hACE2 transgenic mice on days 1, 2 and 3 post inoculation. Repeated measures two-way ANOVA with Tukey corrected multiple comparisons on log10-transformed values, F=16.96, p<0.0001, 4 degrees of freedom. (**b) Total area under the curve** shows cumulative virus levels in swabs.

ANOVA of log10-transformed total peak area with Tukey corrected multiple comparisons, F=7.538, p<0.0001, 4 degrees of freedom. Mice were necropsied on days 5, 6, 7 and 14 post-inoculation as euthanasia criteria were met. Infectious virus levels were measured in (**c**) **lung** and (**d**) **brain** at experimental endpoints. Main effects only model two-way ANOVA on log10-transformed values, F=2.431, p=0.0606, 4 degrees of freedom for lung, F=0.8134, p=0.5229, 4 degrees of freedom for brain. Symbols are individual animals, horizontal lines show geometric mean, and error bars represent geometric standard deviation. n=8-16 per group, 2 combined experiments. LD = limit of detection, AUC = area under the curve. * $p < 0.05$, *** $p < 0.001$, **** $p < 0.0001$.

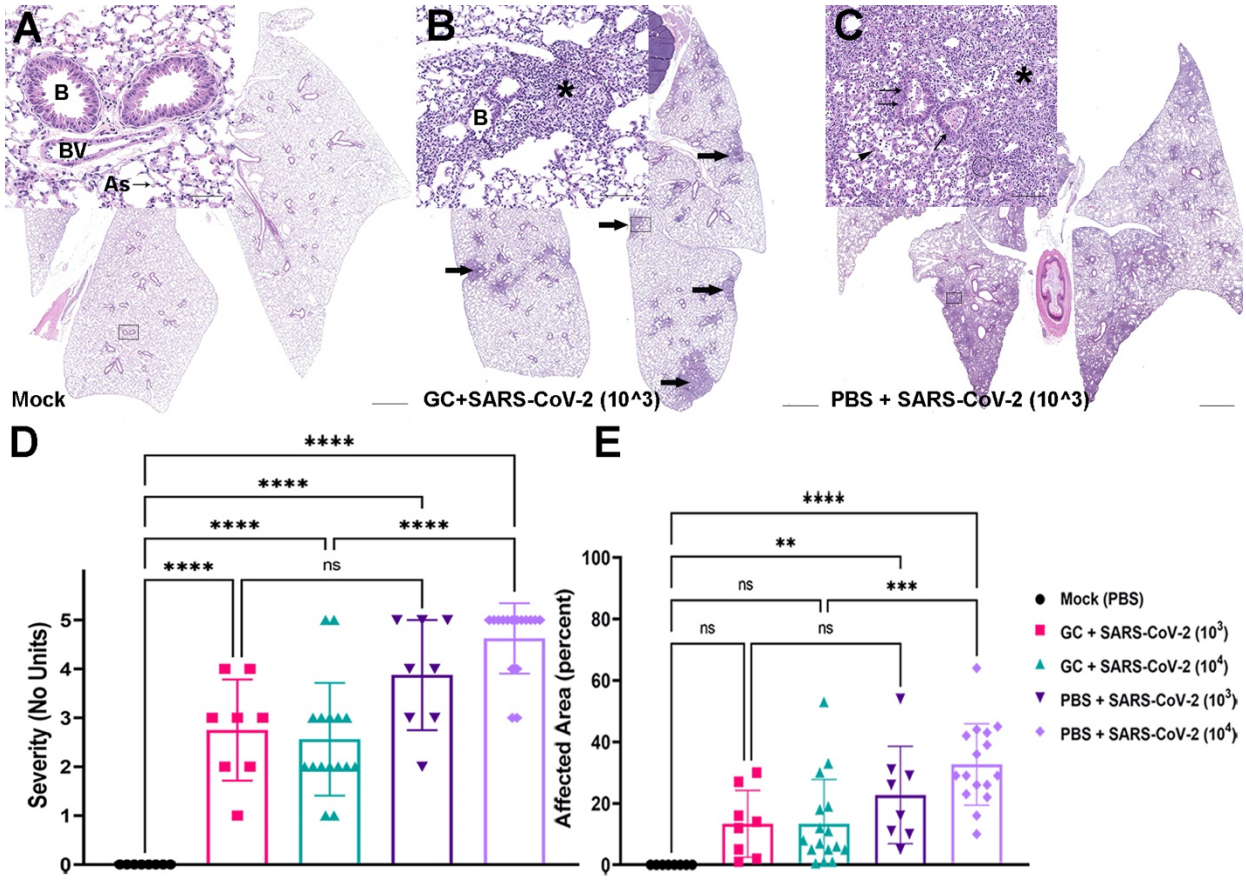

Fig. 3: N-dihydrogalactochitosan reduces histopathology associated with SARS-CoV-2 infection in lungs. Lungs from hACE2 transgenic mice were collected at the time of death, thin sectioned, and hematoxylin and eosin stained for histopathological scoring. Images show representative lungs. **(a) PBS-treated, mock inoculated mouse at day 14**, with normal bronchioles lined by epithelial cells, alveolar septa containing pulmonary capillaries lined by pneumocytes, and a small arteriole are visible in normal lung (inset). **(b) GC + 10^3 PFU SARS-CoV-2 mouse at day 7** with patchy inflammation (black arrows) distributed around airways and affecting approximately 15% of the section and peribronchiolar alveolar septal inflammation composed primarily of lymphocytes and macrophages with scattered multinucleated cells (inset). **(c) PBS + 10^3 PFU SARS-CoV-2 inoculated mouse at day 7** showing widespread, multifocal to coalescing inflammation affecting all lung lobes and approximately 60% of the section. Endotheliitis (circled) and bronchiolar epithelial hyperplasia characterized by

disorganization and piling-up of bronchiolar epithelium with increased mitotic figures (black arrows) is shown in inset. **(d) Lung lesion severity** was scored according to criteria defined in Supplementary Table 1 and the (**e**) **Total affected lung area** was estimated using image analysis software. Scale bars are 2 mm (subgross) and 50 µm (insets). As=alveolar septa, B=bronchioles, Br=bronchus, BV=blood vessel. ** $p < 0.01$, *** $p < 0.001$, **** $p < 0.0001$, ns=not significant. ANOVA, F=35.86, p<0.0001, 4 degrees of freedom (d). ANOVA, F=10.32, p<0.0001, 4 degrees of freedom (e). Symbols are individual animals, bars show the mean, and error bars show the standard deviation, n=8-16 per group, 2 combined experiments.

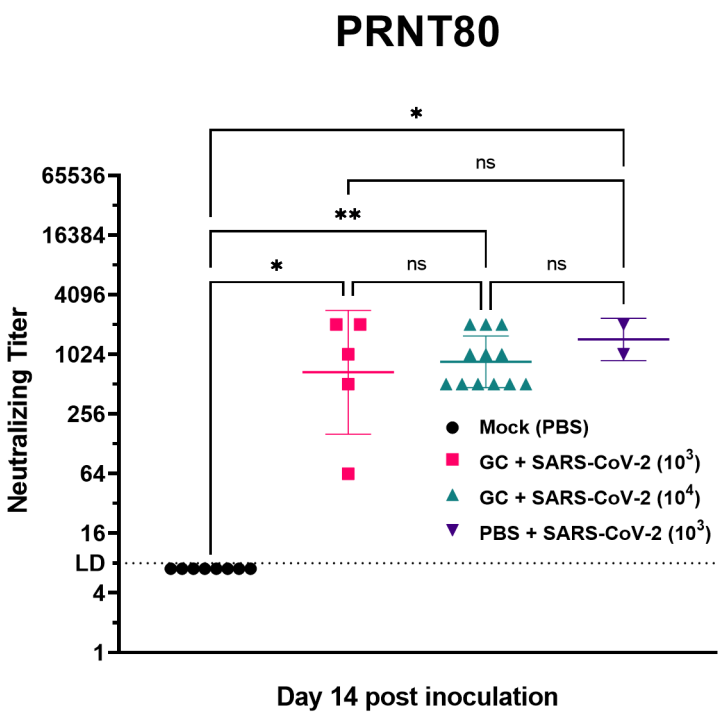

Fig. 4: N-dihydrogalactochitosan treated mice surviving SARS-CoV-2 challenge produce neutralizing antibodies. Neutralizing antibody was assessed by 80% plaque reduction neutralization test (PRNT80) in serum from hACE2 transgenic mice surviving to day 14 post inoculation. No PBS treated mice inoculated with 10^4 PFU SARS-CoV-2 were available for comparison due to uniform mortality. * $p < 0.05$, ** $p < 0.01$, LD = limit of detection. Kruskal-Wallis test with Dunn corrected multiple comparisons, H=17.87, p=0.0005, 3 degrees of freedom. Symbols are individual animals, horizontal lines are geometric mean and error bars show geometric standard deviation, n=2-12 per group, two combined experiments.

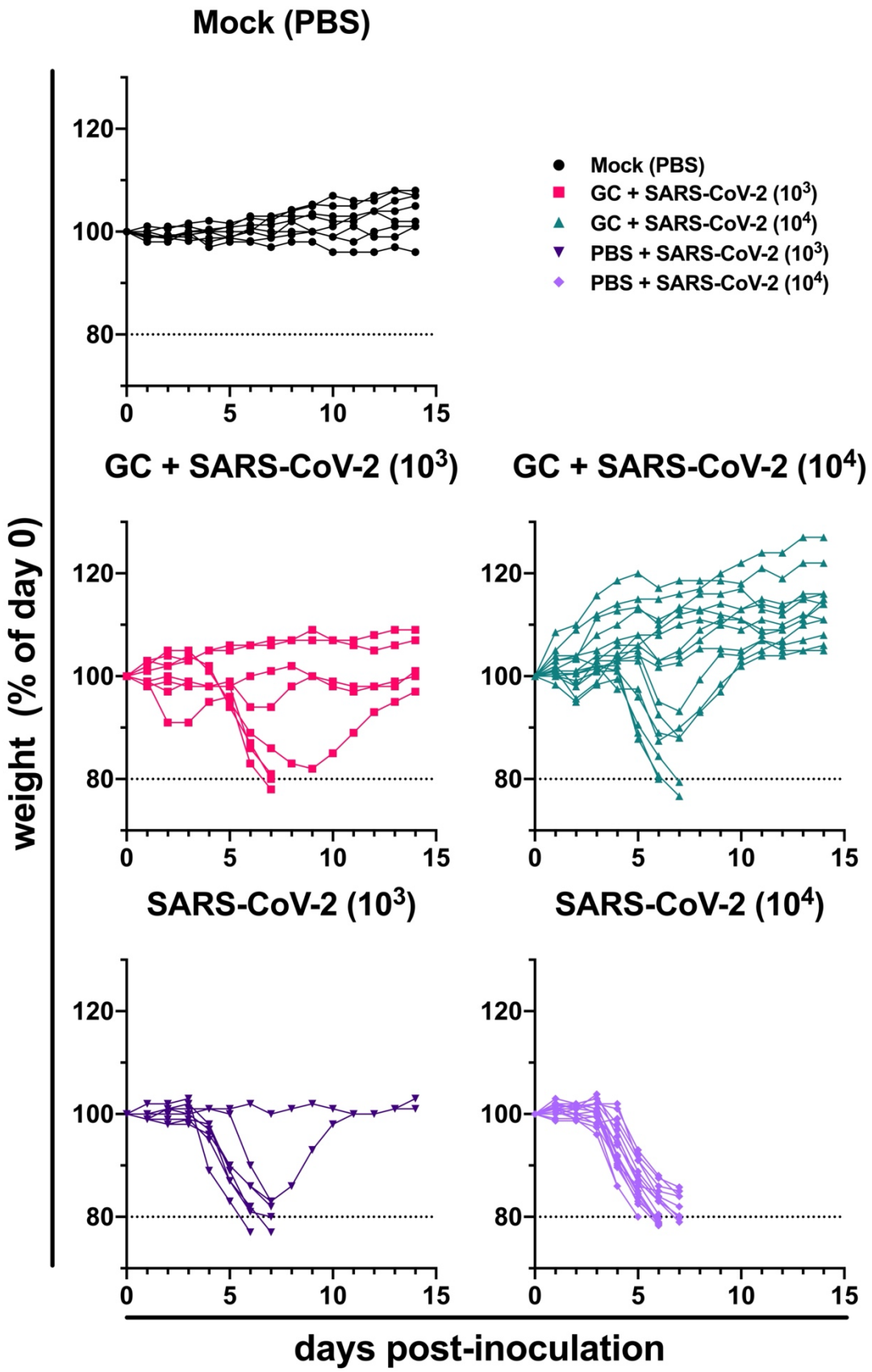
Mock (PBS)
GC + SARS-CoV-2 (10^3)
GC + SARS-CoV-2 (10^4)
SARS-CoV-2 (10^3)
SARS-CoV-2 (10^4)
Mock (PBS)
GC + SARS-CoV-2 (10^3)
GC + SARS-CoV-2 (10^4)
PBS + SARS-CoV-2 (10^3)
PBS + SARS-CoV-2 (10^4)
weight (% of day 0)
days post-inoculation
120
100
80
0
5
10
15

520

521 **Supplementary Fig. 1: N-dihydrogalactochitosan protects mice from SARS-CoV-2 weight**

522 **loss.** Each line shows individual mouse weight as a percentage of their starting weight at the

523 time of challenge.

524

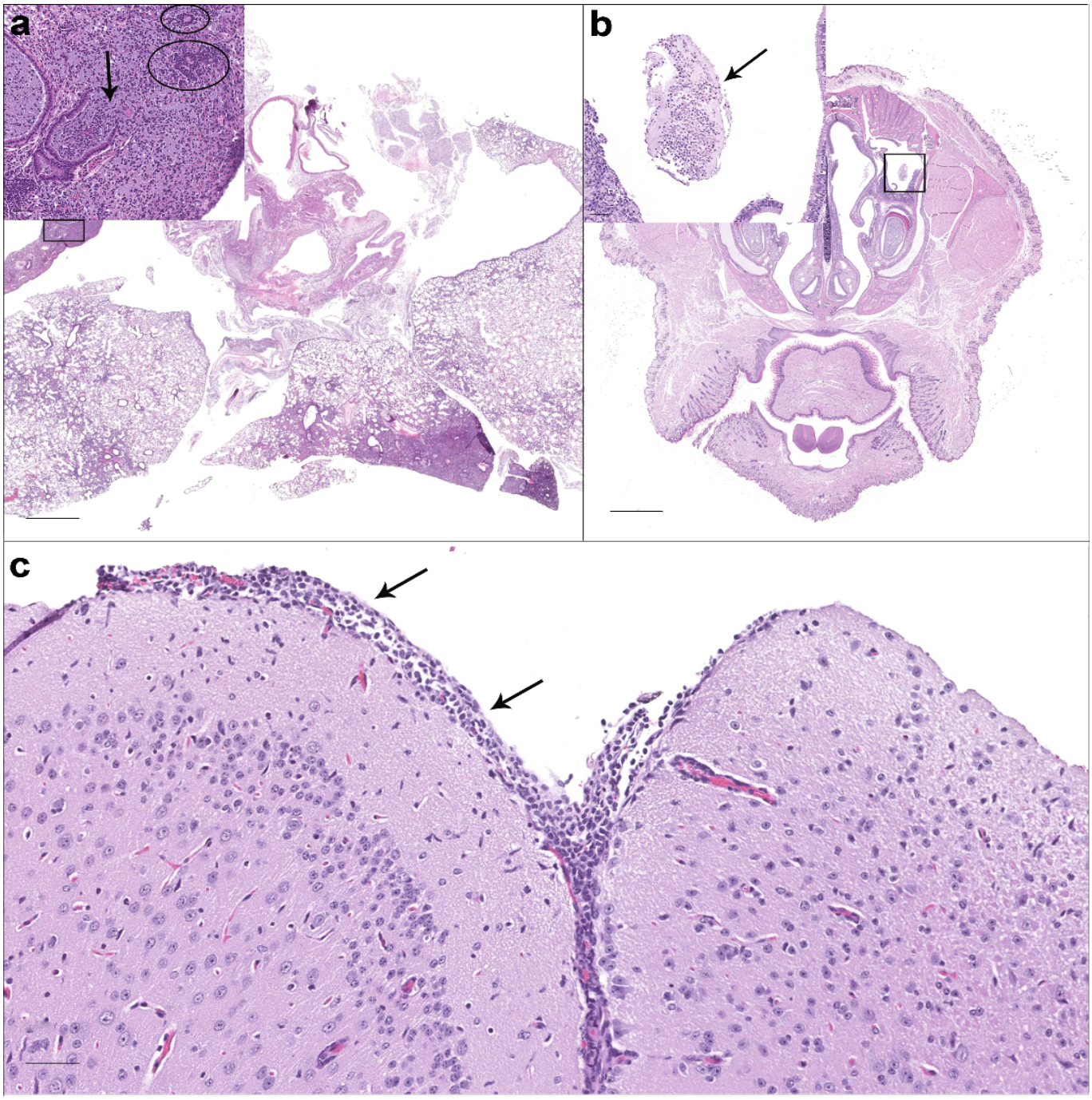

Supplementary Fig. 2: Additional photomicrographs of H&E-stained sections of lung, nasal cavity, and brain of hACE2 mice. **(a) Foreign material in lungs of some intranasally-treated animals.** Lung from a GC-treated 10^4 PFU SARS-CoV-2 inoculated male mouse at 7 days exhibits evidence of a foreign material reaction. Bronchioles are expanded by mucoid material, degenerate neutrophils and necrotic debris, with focal rupture of the bronchiolar wall (arrow),

530 extension of the inflammatory cells into adjacent alveoli, and foci of brightly eosinophilic foreign
531 material surrounded by neutrophils and macrophages (circled) (inset). **(b-c) A subset of GC- or**
532 **PBS-treated SARS-CoV-2 inoculated mice exhibit rhinitis and/or meningeal inflammation**.
533 **(b)** Nasal cavity from a GC-treated 10^4 PFU SARS-CoV-2 inoculated female mouse at 6 days
534 showing a focal exudate (box) composed of degenerate neutrophils and necrotic debris
535 embedded in mucus (inset). **(c)** Brain from a GC-treated 10^3 PFU SARS-CoV-2 inoculated
536 female mouse at 7 days with mild to moderate meningeal inflammation (arrows) composed
537 primarily of lymphocytes with fewer macrophages. Scale bars are 1 mm (subgross) and 50 μm
538 (insets). H&E stain.
539
540
541
542
543
544
545
546
547
548
549
550
551
552
553
554
555

556 **Supplementary Table 1: Histopathology scoring criteria.**

Score		Description
0	none	Within normal limits or rare, scattered lymphocytic infiltrates not observed in control animals but significance questionable (could be background lesion or variation of normal).
1	minimal	Minimal mononuclear inflammation affecting less than 2% of the section. Inflammatory leukocyte infiltration is limited to a perivascular and/or peribronchiolar distribution with no evidence of alveolar or vascular injury.
2	mild	Mild peribronchiolar/perivascular inflammation which may also expand alveoli/alveolar septa, composed primarily of macrophages and lymphocytes (+/- scattered neutrophils); increased alveolar macrophages; alveolar septal architecture largely intact; affects 2-10% of the section; and/or scattered alveolar hemorrhage/fibrin/edema; and/or scattered atypical/multinucleated syncytial cells.
3	moderate	Moderate bronchointerstitial and perivascular inflammation, increased alveolar macrophages, and/or alveolar hemorrhage/fibrin/edema (characterized as above); and/or alveolar damage (characterized by type I pneumocyte necrosis or loss with replacement by hyaline membranes, fibrin, edema, and/or necrotic debris); and/or reparative/regenerative changes (type II pneumocyte hyperplasia, atypical/multinucleated syncytial cells, or fibrosis); lesions affect 10-25% of the section.
4	severe	As above but more widespread inflammation, hemorrhage/fibrin/ edema, and/or alveolar damage/loss of normal septal architecture; and or regenerative changes affecting greater than 25% of the section.
+1		Add 1 point if: Greater than 25% of inflammatory cells are neutrophils; there is significant necrotizing vasculitis, endotheliitis or microthrombi; or if there is significant bronchiolitis, airway epithelial necrosis or hyperplasia.

557

558
559
560
561
562
563
564

565 **REFERENCES**

566

567 1. C. Huang, Y. Wang, X. Li, L. Ren, J. Zhao, Y. Hu, L. Zhang, G. Fan, J. Xu, X. Gu, Z. Cheng,
568 T. Yu, J. Xia, Y. Wei, W. Wu, X. Xie, W. Yin, H. Li, M. Liu, Y. Xiao, H. Gao, L. Guo, J. Xie, G.
569 Wang, R. Jiang, Z. Gao, Q. Jin, J. Wang, B. Cao, Clinical features of patients infected with 2019
570 novel coronavirus in Wuhan, China, *Lancet* (2020), doi:10.1016/S0140-6736(20)30183-5.

571 2. D. Wang, B. Hu, C. Hu, F. Zhu, X. Liu, J. Zhang, B. Wang, H. Xiang, Z. Cheng, Y. Xiong, Y.
572 Zhao, Y. Li, X. Wang, Z. Peng, Clinical Characteristics of 138 Hospitalized Patients with 2019
573 Novel Coronavirus-Infected Pneumonia in Wuhan, China, *JAMA - J. Am. Med. Assoc.* **323**,
574 1061–1069 (2020).

575 3. N. Chen, M. Zhou, X. Dong, J. Qu, F. Gong, Y. Han, Y. Qiu, J. Wang, Y. Liu, Y. Wei, J. Xia,
576 T. Yu, X. Zhang, L. Zhang, Epidemiological and clinical characteristics of 99 cases of 2019
577 novel coronavirus pneumonia in Wuhan, China: a descriptive study, *Lancet* **395**, 507–513
578 (2020).

579 4. F. Zhou, T. Yu, R. Du, G. Fan, Y. Liu, Z. Liu, J. Xiang, Y. Wang, B. Song, X. Gu, L. Guan, Y.
580 Wei, H. Li, X. Wu, J. Xu, S. Tu, Y. Zhang, H. Chen, B. Cao, Clinical course and risk factors for
581 mortality of adult inpatients with COVID-19 in Wuhan, China: a retrospective cohort study,
582 *Lancet* **395**, 1054–1062 (2020).

583 5. J. Hellmuth, T. A. Barnett, B. M. Asken, J. D. Kelly, L. Torres, M. L. Stephens, B.
584 Greenhouse, J. N. Martin, F. C. Chow, S. G. Deeks, M. Greene, B. L. Miller, W. Annan, T. J.
585 Henrich, M. J. Peluso, Persistent COVID-19-associated neurocognitive symptoms in non-
586 hospitalized patients, *J. Neurovirol.* **27**, 191–195 (2021).

587 6. E. L. Graham, J. R. Clark, Z. S. Orban, P. H. Lim, A. L. Szymanski, C. Taylor, R. M. DiBiase,
588 D. T. Jia, R. Balabanov, S. U. Ho, A. Batra, E. M. Liotta, I. J. Koralnik, Persistent neurologic
589 symptoms and cognitive dysfunction in non-hospitalized Covid-19 “long haulers,” *Ann. Clin.*
590 *Transl. Neurol.* (2021), doi:10.1002/acn3.51350.

591 7. R. Lu, X. Zhao, J. Li, P. Niu, B. Yang, H. Wu, W. Wang, H. Song, B. Huang, N. Zhu, Y. Bi, X.

592 Ma, F. Zhan, L. Wang, T. Hu, H. Zhou, Z. Hu, W. Zhou, L. Zhao, J. Chen, Y. Meng, J. Wang, Y.
593 Lin, J. Yuan, Z. Xie, J. Ma, W. J. Liu, D. Wang, W. Xu, E. C. Holmes, G. F. Gao, G. Wu, W.
594 Chen, W. Shi, W. Tan, Genomic characterisation and epidemiology of 2019 novel coronavirus:
595 implications for virus origins and receptor binding, *Lancet* **395**, 565–574 (2020).
596 8. P. Zhou, X. Lou Yang, X. G. Wang, B. Hu, L. Zhang, W. Zhang, H. R. Si, Y. Zhu, B. Li, C. L.
597 Huang, H. D. Chen, J. Chen, Y. Luo, H. Guo, R. Di Jiang, M. Q. Liu, Y. Chen, X. R. Shen, X.
598 Wang, X. S. Zheng, K. Zhao, Q. J. Chen, F. Deng, L. L. Liu, B. Yan, F. X. Zhan, Y. Y. Wang, G.
599 F. Xiao, Z. L. Shi, A pneumonia outbreak associated with a new coronavirus of probable bat
600 origin, *Nature* **579**, 270–273 (2020).
601 9. S. S. Lakdawala, V. D. Menachery, The search for a COVID-19 animal model, *Science (80-.*
602 *).* **368**, 942–943 (2020).
603 10. C. Muñoz-Fontela, W. E. Dowling, S. G. P. Funnell, P. S. Gsell, A. X. Riveros-Balta, R. A.
604 Albrecht, H. Andersen, R. S. Baric, M. W. Carroll, M. Cavaleri, C. Qin, I. Crozier, K. Dallmeier, L.
605 de Waal, E. de Wit, L. Delang, E. Dohm, W. P. Duprex, D. Falzarano, C. L. Finch, M. B.
606 Frieman, B. S. Graham, L. E. Gralinski, K. Guilfoyle, B. L. Haagmans, G. A. Hamilton, A. L.
607 Hartman, S. Herfst, S. J. F. Kaptein, W. B. Klimstra, I. Knezevic, P. R. Krause, J. H. Kuhn, R. Le
608 Grand, M. G. Lewis, W. C. Liu, P. Maisonnasse, A. K. McElroy, V. Munster, N. Oreshkova, A. L.
609 Rasmussen, J. Rocha-Pereira, B. Rockx, E. Rodríguez, T. F. Rogers, F. J. Salguero, M.
610 Schotsaert, K. J. Stittelaar, H. J. Thibaut, C. Te Tseng, J. Vergara-Alert, M. Beer, T. Brasel, J. F.
611 W. Chan, A. García-Sastre, J. Neyts, S. Perlman, D. S. Reed, J. A. Richt, C. J. Roy, J. Segalés,
612 S. S. Vasan, A. M. Henao-Restrepo, D. H. Barouch, Animal models for COVID-19, *Nature* **586**,
613 509–515 (2020).
614 11. P. B. McCray, L. Pewe, C. Wohlford-Lenane, M. Hickey, L. Manzel, L. Shi, J. Netland, H. P.
615 Jia, C. Halabi, C. D. Sigmund, D. K. Meyerholz, P. Kirby, D. C. Look, S. Perlman, Lethal
616 Infection of K18-hACE2 Mice Infected with Severe Acute Respiratory Syndrome Coronavirus, *J.*
617 *Virol.* (2007), doi:10.1128/jvi.02012-06.

618 12. E. S. Winkler, A. L. Bailey, N. M. Kafai, S. Nair, B. T. McCune, J. Yu, J. M. Fox, R. E. Chen,
619 J. T. Earnest, S. P. Keeler, J. H. Ritter, L. I. Kang, S. Dort, A. Robichaud, R. Head, M. J.
620 Holtzman, M. S. Diamond, SARS-CoV-2 infection of human ACE2-transgenic mice causes
621 severe lung inflammation and impaired function, *Nat. Immunol.* **21**, 1327–1335 (2020).
622 13. J. Zheng, L. Y. R. Wong, K. Li, A. K. Verma, M. E. Ortiz, C. Wohlford-Lenane, M. R.
623 Leidinger, C. M. Knudson, D. K. Meyerholz, P. B. McCray, S. Perlman, COVID-19 treatments
624 and pathogenesis including anosmia in K18-hACE2 mice, *Nature* **589**, 603–607 (2021).
625 14. Symptoms of COVID-19 | CDC (available at https://www.cdc.gov/coronavirus/2019-
626 ncov/symptoms-testing/symptoms.html).
627 15. FDA Issues Emergency Use Authorization for Third COVID-19 Vaccine | FDA (available at
628 https://www.fda.gov/news-events/press-announcements/fda-issues-emergency-use-
629 authorization-third-covid-19-vaccine).
630 16. Coronavirus disease (COVID-19): Herd immunity, lockdowns and COVID-19 (available at
631 https://www.who.int/news-room/q-a-detail/herd-immunity-lockdowns-and-covid-19).
632 17. A. Rhoades, *Veklury (remdesivir) EUA Letter of Approval, reissued 10/22/2020* (2020).
633 18. J. H. Beigel, K. M. Tomashek, L. E. Dodd, A. K. Mehta, B. S. Zingman, A. C. Kalil, E.
634 Hohmann, H. Y. Chu, A. Luetkemeyer, S. Kline, D. Lopez de Castilla, R. W. Finberg, K.
635 Dierberg, V. Tapson, L. Hsieh, T. F. Patterson, R. Paredes, D. A. Sweeney, W. R. Short, G.
636 Touloumi, D. C. Lye, N. Ohmagari, M. Oh, G. M. Ruiz-Palacios, T. Benfield, G. Fätkenheuer, M.
637 G. Kortepeter, R. L. Atmar, C. B. Creech, J. Lundgren, A. G. Babiker, S. Pett, J. D. Neaton, T.
638 H. Burgess, T. Bonnett, M. Green, M. Makowski, A. Osinusi, S. Nayak, H. C. Lane, Remdesivir
639 for the Treatment of Covid-19 — Final Report, *N. Engl. J. Med.* **383**, 1813–1826 (2020).
640 19. WHO recommends against the use of remdesivir in COVID-19 patients (available at
641 https://www.who.int/news-room/feature-stories/detail/who-recommends-against-the-use-of-
642 remdesivir-in-covid-19-patients).
643 20. Food and Drug Administration, *FDA Combating COVID-19 With Therapeutics* (2020)

644 (available at https://www.fda.gov/media/136832/download).
645 21. S. N. Chirkov, The antiviral activity of chitosan (review)*Appl. Biochem. Microbiol.* **38**, 1–8
646 (2002).
647 22. M. Mehrabi, H. Montazeri, M. N. Dounighi, A. Rashti, R. Vakili-Ghartavol, Chitosan-based
648 nanoparticles in mucosal vaccine delivery*Arch. Razi Inst.* **73**, 165–176 (2018).
649 23. X. Li, M. Min, N. Du, Y. Gu, T. Hode, M. Naylor, D. Chen, R. E. Nordquist, W. R. Chen,
650 Chitin, chitosan, and glycated chitosan regulate immune responses: The novel adjuvants for
651 cancer vaccine*Clin. Dev. Immunol.* **2013** (2013), doi:10.1155/2013/387023.
652 24. J. Mudgal, P. P. Mudgal, M. Kinra, R. Raval, Immunomodulatory role of chitosan-based
653 nanoparticles and oligosaccharides in cyclophosphamide-treated mice, *Scand. J. Immunol.* **89**,
654 e12749 (2019).
655 25. T. D. Carroll, S. Jegaskanda, S. R. Matzinger, L. Fritts, M. B. McChesney, S. J. Kent, J.
656 Fairman, C. J. Miller, A lipid/DNA adjuvant-inactivated influenza virus vaccine protects rhesus
657 macaques from uncontrolled virus replication afer heterosubtypic influenza a virus challenge, *J.*
658 *Infect. Dis.* (2018), doi:10.1093/infdis/jiy238.
659 26. X. Lei, X. Dong, R. Ma, W. Wang, X. Xiao, Z. Tian, C. Wang, Y. Wang, L. Li, L. Ren, F. Guo,
660 Z. Zhao, Z. Zhou, Z. Xiang, J. Wang, Activation and evasion of type I interferon responses by
661 SARS-CoV-2, *Nat. Commun.* **11** (2020), doi:10.1038/s41467-020-17665-9.
662 27. H. Xia, Z. Cao, X. Xie, X. Zhang, J. Y. C. Chen, H. Wang, V. D. Menachery, R. Rajsbaum,
663 P. Y. Shi, Evasion of Type I Interferon by SARS-CoV-2, *Cell Rep.* **33** (2020),
664 doi:10.1016/j.celrep.2020.108234.
665 28. M. S. Ribero, N. Jouvenet, M. Dreux, S. Nisole, Interplay between SARS-CoV-2 and the
666 type I interferon response*PLoS Pathog.* **16** (2020), doi:10.1371/journal.ppat.1008737.
667 29. M. Zheng, D. Qu, H. Wang, Z. Sun, X. Liu, J. Chen, C. Li, X. Li, Z. Chen, Intranasal
668 Administration of Chitosan Against Influenza A (H7N9) Virus Infection in a Mouse Model, *Sci.*
669 *Rep.* **6** (2016), doi:10.1038/srep28729.

670 30. X. Wang, W. Zhang, F. Liu, M. Zheng, D. Zheng, T. Zhang, Y. Yi, Y. Ding, J. Luo, C. Dai, H.
671 Wang, B. Sun, Z. Chen, Intranasal immunization with live attenuated influenza vaccine plus
672 chitosan as an adjuvant protects mice against homologous and heterologous virus challenge,
673 *Arch. Virol.* **157**, 1451–1461 (2012).
674 31. B. Choi, D. H. Jo, A. K. M. M. Anower, S. M. S. Islam, S. Sohn, Chitosan as an
675 Immunomodulating Adjuvant on T-Cells and Antigen-Presenting Cells in Herpes Simplex Virus
676 Type 1 Infection, *Mediators Inflamm.* **2016** (2016), doi:10.1155/2016/4374375.
677 32. W. R. Chen, R. Carubelli, H. Liu, R. E. Nordquist, Laser immunotherapy: A novel treatment
678 modality for metastatic tumors, *Appl. Biochem. Biotechnol. - Part B Mol. Biotechnol.* **25**, 37–43
679 (2003).
680 33. S. Song, F. Zhou, R. E. Nordquist, R. Carubelli, H. Liu, W. R. Chen, Glycated chitosan as a
681 new non-toxic immunological stimulant Glycated chitosan immunological stimulant,
682 *Immunopharmacol. Immunotoxicol.* **31**, 202–208 (2009).
683 34. I. Zizzari, C. Napoletano, F. Battisti, H. Rahimi, S. Caponnetto, L. Pierelli, M. Nuti, A.
684 Rughetti, MGL Receptor and Immunity: When the Ligand Can Make the Difference, *J. Immunol.*
685 *Res.* **2015** (2015), doi:10.1155/2015/450695.
686 35. M. Korbelik, J. Banáth, W. Zhang, T. Hode, S. Lam, P. Gallagher, J. Zhao, H. Zeng, W.
687 Chen, N-dihydrogalactochitosan-supported tumor control by photothermal therapy and
688 photothermal therapy-generated vaccine, *J. Photochem. Photobiol. B.* **204** (2020),
689 doi:10.1016/J.JPHOTOBIOL.2020.111780.
690 36. M. Korbelik, T. Hode, S. S. K. Lam, W. R. Chen, Novel Immune Stimulant Amplifies Direct
691 Tumoricidal Effect of Cancer Ablation Therapies and Their Systemic Antitumor Immune
692 Efficacy*Cells* **10** (2021), doi:10.3390/cells10030492.
693 37. S. Qi, L. Lu, F. Zhou, Y. Chen, M. Xu, L. Chen, X. Yu, W. R. Chen, Z. Zhang, Neutrophil
694 infiltration and whole-cell vaccine elicited by N-dihydrogalactochitosan combined with NIR
695 phototherapy to enhance antitumor immune response and T cell immune memory, *Theranostics*

10, 1814–1832 (2020).

38. F. Zhou, J. Yang, Y. Zhang, M. Liu, M. L. Lang, M. Li, W. R. Chen, Local phototherapy synergizes with immunoadjuvant for treatment of pancreatic cancer through induced immunogenic tumor vaccine, *Clin. Cancer Res.* **24**, 5335–5346 (2018).

39. A. El-Hussein, S. S. K. Lam, J. Raker, W. R. Chen, M. R. Hamblin, N-dihydrogalactochitosan as a potent immune activator for dendritic cells, *J. Biomed. Mater. Res. - Part A* **105**, 963–972 (2017).

40. A. R. Hoover, K. Liu, C. I. Devette, J. R. Krawic, C. L. West, D. Medcalf, A. L. Welm, X.-H. Sun, W. H. Hildebrand, W. R. Chen, ScRNA-seq reveals tumor microenvironment remodeling induced by local intervention-based immunotherapy, *bioRxiv* , 2020.10.02.323006 (2020).

41. C. Brown, J. Vostok, H. Johnson, M. Burns, R. Gharpure, S. Sami, R. Sabo, N. Hall, A. Foreman, P. Schubert, G. Gallagher, T. Fink, L. Madoff, S. Gabriel, B. MacInnis, D. Park, K. Siddle, V. Harik, D. Arvidson, T. Brock-Fisher, M. Dunn, A. Kearns, A. Laney, Outbreak of SARS-CoV-2 Infections, Including COVID-19 Vaccine Breakthrough Infections, Associated with Large Public Gatherings - Barnstable County, Massachusetts, July 2021, *MMWR. Morb. Mortal. Wkly. Rep.* **70**, 1059–1062 (2021).

42. B. Bellich, I. D'Agostino, S. Semeraro, A. Gamini, A. Cesàro, "The Good, the Bad and the Ugly" of Chitosans, *Mar. Drugs* **14** (2016), doi:10.3390/MD14050099.

43. K. Jayathilakan, K. Sultana, K. Radhakrishna, A. S. Bawa, Utilization of byproducts and waste materials from meat, poultry and fish processing industries: A review*J. Food Sci. Technol.* **49**, 278–293 (2012).

44. N. A. Negm, H. H. H. Hefni, A. A. A. Abd-Elaal, E. A. Badr, M. T. H. Abou Kana, Advancement on modification of chitosan biopolymer and its potential applications*Int. J. Biol. Macromol.* **152**, 681–702 (2020).

45. H. Mokhtar, L. Biffar, S. Somavarapu, J. P. Frossard, S. McGowan, M. Pedrera, R. Strong, J. C. Edwards, M. Garcia-Durán, M. J. Rodriguez, G. R. Stewart, F. Steinbach, S. P. Graham,

722 Evaluation of hydrophobic chitosan-based particulate formulations of porcine reproductive and
723 respiratory syndrome virus vaccine candidate T cell antigens, *Vet. Microbiol.* **209**, 66–74 (2017).
724 46. S. Shim, H. E. Park, S. H. Soh, Y. Bin Im, H. S. Yoo, Induction of Th2 response through
725 TLR2-mediated MyD88-dependent pathway in human microfold cells stimulated with chitosan
726 nanoparticles loaded with Brucella abortus Mdh, *Microb. Pathog.* **142** (2020),
727 doi:10.1016/j.micpath.2020.104040.
728 47. X. Zhang, K. Wu, D. Wang, X. Yue, D. Song, Y. Zhu, J. Wu, Nucleocapsid protein of SARS-
729 CoV activates interleukin-6 expression through cellular transcription factor NF-κB, *Virology* **365**,
730 324–335 (2007).
731 48. D. Blanco-Melo, B. E. Nilsson-Payant, W. C. Liu, S. Uhl, D. Hoagland, R. Møller, T. X.
732 Jordan, K. Oishi, M. Panis, D. Sachs, T. T. Wang, R. E. Schwartz, J. K. Lim, R. A. Albrecht, B.
733 R. tenOever, Imbalanced Host Response to SARS-CoV-2 Drives Development of COVID-19,
734 *Cell* **181**, 1036-1045.e9 (2020).
735 49. C. Pyle, F. Uwadiae, D. Swieboda, J. Harker, Early IL-6 signalling promotes IL-27
736 dependent maturation of regulatory T cells in the lungs and resolution of viral immunopathology,
737 *PLoS Pathog.* **13** (2017), doi:10.1371/JOURNAL.PPAT.1006640.
738 50. C. L. Bueter, C. K. Lee, V. A. K. Rathinam, G. J. Healy, C. H. Taron, C. A. Specht, S. M.
739 Levitz, Chitosan but not chitin activates the inflammasome by a mechanism dependent upon
740 phagocytosis, *J. Biol. Chem.* **286**, 35447–35455 (2011).
741 51. E. C. Carroll, L. Jin, A. Mori, N. Muñoz-Wolf, E. Oleszycka, H. B. T. Moran, S. Mansouri, C.
742 P. McEntee, E. Lambe, E. M. Agger, P. Andersen, C. Cunningham, P. Hertzog, K. A. Fitzgerald,
743 A. G. Bowie, E. C. Lavelle, The Vaccine Adjuvant Chitosan Promotes Cellular Immunity via DNA
744 Sensor cGAS-STING-Dependent Induction of Type I Interferons, *Immunity* **44**, 597–608 (2016).
745 52. B. Sun, S. Yu, D. Zhao, S. Guo, X. Wang, K. Zhao, Polysaccharides as vaccine
746 adjuvants*Vaccine* **36**, 5226–5234 (2018).
747 53. R. C. Read, S. C. Naylor, C. W. Potter, J. Bond, I. Jabbal-Gill, A. Fisher, L. Illum, R.

Jennings, Effective nasal influenza vaccine delivery using chitosan, *Vaccine* **23**, 4367–4374 (2005).

54. D. Elieh Ali Komi, L. Sharma, C. S. Dela Cruz, Chitin and Its Effects on Inflammatory and Immune Responses*Clin. Rev. Allergy Immunol.* **54**, 213–223 (2018).

55. S. Bashiri, P. Koirala, I. Toth, M. Skwarczynski, Carbohydrate immune adjuvants in subunit vaccines*Pharmaceutics* **12**, 1–33 (2020).

56. C. L. Bueter, C. A. Specht, S. M. Levitz, Innate Sensing of Chitin and Chitosan, *PLoS Pathog.* **9** (2013), doi:10.1371/journal.ppat.1003080.

57. J. Seetharaman, A. Kfanigsberg, R. Slaaby, H. Leffler, S. H. Barondes, J. M. Rini, X-ray crystal structure of the human galectin-3 carbohydrate recognition domain at 2.1-Å resolution, *J. Biol. Chem.* **273**, 13047–13052 (1998).

58. T. Semeňuk, P. Krist, J. Pavlíček, K. Bezouška, M. Kuzma, P. Novák, V. Křen, Synthesis of chitooligomer-based glycoconjugates and their binding to the rat natural killer cell activation receptor NKR-P1, *Glycoconj. J.* **18**, 817–826 (2001).

59. F. Zhou, S. Wu, S. Song, W. R. Chen, D. E. Resasco, D. Xing, Antitumor immunologically modified carbon nanotubes for photothermal therapy, *Biomaterials* **33**, 3235–3242 (2012).

60. R. J. Nevagi, Z. G. Khalil, W. M. Hussein, J. Powell, M. R. Batzloff, R. J. Capon, M. F. Good, M. Skwarczynski, I. Toth, Polyglutamic acid-trimethyl chitosan-based intranasal peptide nano-vaccine induces potent immune responses against group A streptococcus, *Acta Biomater.* **80**, 278–287 (2018).

61. F. Micoli, P. Costantino, R. Adamo, Potential targets for next generation antimicrobial glycoconjugate vaccines*FEMS Microbiol. Rev.* **42**, 388–423 (2018).